Far-Infrared and Sub-Millimeter Observations and Physical Models of the Reflection Nebula Ced 201

Ciska Kemper¹

Leiden Observatory, P.O. Box 9513, 2300 RA Leiden, The Netherlands

Marco Spaans²

Harvard-Smithsonian Center for Astrophysics, Cambridge, MA 02138, USA

David J. Jansen

Leiden Observatory, P.O. Box 9513, 2300 RA Leiden, The Netherlands

Michiel R. Hogerheijde³

Leiden Observatory, P.O. Box 9513, 2300 RA Leiden, The Netherlands

Ewine F. van Dishoeck

Leiden Observatory, P.O. Box 9513, 2300 RA Leiden, The Netherlands

Xander G. G. M. Tielens

Kapteyn Institute, P.O. Box 800, 9700 AV Groningen, The Netherlands

Received ______; accepted _____

¹Currently at the University of Amsterdam, Kruislaan 403, Amsterdam, The Netherlands

²Hubble Fellow

³Currently at the University of California in Berkeley, 601 Campbell Hall, CA 94720, USA

ABSTRACT

ISO [C II] 158 μ m, [O I] 63 μ m, and H₂ 9 and 17 μ m observations are presented of the reflection nebula Ced 201, which is a photon-dominated region illuminated by a B9.5 star with a color temperature of 10,000 K (a cool PDR). In combination with ground based [C I] 609 μ m, CO, ¹³CO, CS and HCO⁺ data, the carbon budget and physical structure of the reflection nebula are constrained. The obtained data set is the first one to contain all important cooling lines of a cool PDR, and allows a comparison to be made with classical PDRs. To this effect one- and three-dimensional PDR models are presented which incorporate the physical characteristics of the source, and are aimed at understanding the dominant heating processes of the cloud. The contribution of very small grains to the photo-electric heating rate is estimated from these models and used to constrain the total abundance of PAHs and small grains. Observations of the pure rotational H₂ lines with ISO, in particular the S(3) line, indicate the presence of a small amount of very warm \sim 330 K molecular gas. This gas cannot be accommodated by the presented models.

subject headings: ISM: clouds - ISM: Ced 201 - ISM: molecules - molecular processes - reflection nebulae

1. Introduction

A major problem concerning the interstellar medium and circumstellar regions remains the identification of the dominant gas heating source. The best current model is photo-electric emission by dust grains following irradiation by ultraviolet photons. The ejected electrons carry an excess kinetic energy of a few eV which is transferred to the gas by elastic collisions with H and H₂. The efficiency of this photo-electric heating for various densities and illuminating radiation fields has been the subject of many investigations (Hollenbach & Tielens 1997; Spaans et al. 1994; and references therein). Bakes & Tielens (1994) presented calculations for the contribution of Very Small Grains (VSGs) and large molecules like polycyclic hydrocarbons (PAHs) to the total heating rate. To establish a firm theoretical basis for interstellar heating, one therefore has to constrain the abundance of these putative species.

In this work, Infrared Space Observatory (ISO) and ground-based observations are presented of the reflection nebula Ced 201. Since the illuminating star has an effective temperature of 10,000 K, Ced 201 qualifies as a cool PDR. That is, the relatively soft impinging radiation field decreases the photo-electric heating rate, leading to cooler temperatures. Furthermore, the resulting photo-electric heating rate has larger contributions from grain species with low ionization potentials and negative (or small positive) charges (Bakes & Tielens 1994). Ced 201 is thus ideally suited to investigate the role of PAHs in the photo-electric heating process (Spaans et al. 1994).

Most PDR models to date are constructed for classical PDRs, i.e. PDRs illuminated by O or early-type B stars. The aim of this study is to use a complete set of atomic and molecular diagnostics to constrain the total cooling, the density, the extinction, and the illuminating radiation field of a cool PDR. If the physical and chemical structure of the source can be determined consistent with the observations through PDR models, then

it is possible to estimate the contribution of VSGs and PAHs to the total photo-electric heating rate. ISO offers a new opportunity to probe the physics and chemistry of PDRs by observations of the major cooling lines [C II] 158 μ m and [O I] 63 μ m with the Long Wavelength Spectrometer (LWS) and searches for the pure rotational lines of H₂ with the Short Wavelength Spectrometer (SWS). The latter lines provide important constraints on the amount of warm gas in the source, which may not be explained by current models (Timmerman et al. 1996). Searches of these LWS and SWS lines in weak, extended sources such as discussed here have not been possible previously with airborne observatories.

2. Observations

Cederblad 201 is associated with BD +69°1231, a main sequence star of spectral type B9.5 and an effective temperature of 10,000 K. The source is located toward $\alpha = 22:12:14$ and $\delta = 70:00:11$ (Epoch 1950) and lies at a distance of approximately 420 pc (Casey 1991). In this study an extended set of observations of Ced 201 is presented. The source is mapped around the offset position in 12 CO $2 \rightarrow 1$ and $3 \rightarrow 2$ line emission. Additional observations of line transitions of other species are performed at the maximum of the 12 CO $2 \rightarrow 1$ emission. The most important observations are obtained with the James Clerk Maxwell Telescope⁴ (JCMT) and ISO, and are presented in the following sections after the NRAO results.

⁴The James Clerk Maxwell Telescope is operated by the Joint Astronomy Centre, Hilo (Hawaii), on behalf of the UK Particle Physics and Astronomy Research Council, the Netherlands Organization for Scientific Research (NWO) and the National Research Council of Canada.

2.1. NRAO Observations

Single dish observations of the HCO⁺ 1-0 and CS 2-1 lines were made in June 1996 with the NRAO 12m telescope on Kitt peak ⁵. The adopted receiver was the 3mm SIS dual channel mixer. For the back end, the Hybrid Spectrometer was placed in dual channel mode with a resolution of 47.9 KHz (0.16 km s⁻¹). The beam width is 63" FWHM and the main beam efficiency $\eta_{\rm MB} = 0.86$. Pointing is accurate to 10" in azimuth and 5" in elevation. A weak detection of HCO⁺ 1 \rightarrow 0 was found, but the CS 2 \rightarrow 1 line was not detected (see Table 2).

2.2. JCMT Observations

Observations of the ^{12}CO 2 \rightarrow 1 and 3 \rightarrow 2, ^{13}CO 2 \rightarrow 1 and 3 \rightarrow 2, ^{18}O 2 \rightarrow 1, HCO⁺ 3 \rightarrow 2, and [C I] (492 GHz/609 μ m) line transitions were performed in three different wavelength bands. The front-end receivers, the telescope beam sizes, and the efficiencies at the various frequencies are shown in Table 1. The main beam efficiencies η_{MB} were determined from observations of planets by the JCMT staff. All observations were obtained in the 125 MHz configuration, corresponding to a channel width of 0.078 MHz. For these high resolution spectra, the Digital Autocorrelating Spectrometer (DAS) at the back-end of the receiver was used. All observations were made in position switching mode, using an offset of 30′, 45′ or 90′ in azimuth. In this mode, the telescope integrates at the source position for 30 seconds and then switches to an emission-free position on the sky. The difference between these two signals yields the actual source contribution, assuming the atmospheric conditions do not vary significantly on the time scale of a minute. Low

⁵The National Radio Astronomical Observatory is operated by Associated Universities, Inc., under contract with the U.S. National Science Foundation.

order polynomial baseline fits were adopted in the reduction.

 $\label{eq:Table 1} \ensuremath{\text{Table 1}}$ Technical Details of the JCMT

Receiver	Frequency	$\eta_{ m MB}$	$\theta_{\rm beam}$ (")
RxA2	$230~\mathrm{GHz}$	0.69 ± 0.03	21 ± 2
RxB3i	$345~\mathrm{GHz}$	0.58 ± 0.02	14.1 ± 0.5
RxC2	$460~\mathrm{GHz}$	0.52 ± 0.05	10.9 ± 0.5

Table 2 shows an overview of the line transitions observed at the offset position (0'',0''), and Figure 1 shows the ^{12}CO 2 \rightarrow 1 and 3 \rightarrow 2 line emission maps. Most line profiles can be fitted with a Gaussian at $V_{\text{LSR}} = -4.9 \text{ km s}^{-1}$, although in several spectra a smaller peak at $V_{\text{LSR}} = -5.9 \text{ km s}^{-1}$ also occurs. This study will focus on the emission at $V_{\text{LSR}} = -4.9 \text{ km s}^{-1}$. For Ced 201, the ^{12}CO line profiles do not exhibit the characteristic double-peaked shape of self-absorption, except for a few offset positions, located near the edge of the mapped regions, which are not associated with the central PDR. Therefore, it can be concluded that the illuminating star is located between the observer and the central cloud, heating the gas from the outside.

 $\label{eq:Table 2} Table \ 2$ Submillimeter Observations of Ced 201

Line	I	$T_{peak}^{a,b}$	ΔV	V_{LSR}	r.m.s. ^c
	${\rm K~km~s^{-1}}$	K	$\rm km\ s^{-1}$	$\rm km\ s^{-1}$	K
$\mathrm{HCO^{+}}\ 1 \rightarrow 0$	1	0.15	0.85	-5	0.03
$CS\ 2\to 1$	• • •	< 0.03			0.03
$^{12}\mathrm{CO}\ 2 \to 1$	21.3	23.2	0.86	-4.9	0.53
	7.6	6.8	1.1	-5.9	0.53
$^{12}\mathrm{CO}\ 3 \rightarrow 2$	25.3	33.1	0.72	-4.9	0.94
	7.8	6.8	1.1	-5.9	0.94
$^{13}\mathrm{CO}~2 \rightarrow 1$	5.4	6.9	0.73	-4.9	0.71
	1.7	1.5	1.1	-5.9	0.71
$^{13}\mathrm{CO}\ 3 \rightarrow 2$	3.9	5.5	0.66	-4.9	1.0
		< 0.64		-5.9	0.64
$\mathrm{C^{18}O}\ 2 \to 1$		< 0.09			0.09
$\mathrm{HCO^{+}}\ 3 \rightarrow 2$		< 0.08			0.08
[C I] (609 μ m)		<1.3			1.3

^b In case of no detection, the upper limit, obtained by Hanning smoothing once, is shown.

2.3. ISO Observations

Observations of the fine-structure lines of neutral oxygen [O I] and ionized carbon [C II], as well as the pure rotational transitions of molecular hydrogen have been performed by ISO. The LWS (Clegg et al. 1996) AOT02 grating mode was used to obtain spectra of

 $^{^{\}rm c}$ Measured per channel of 0.078 MHz.

the [O I] (63 μ m), [O I] (145 μ m) and [C II] (158 μ m) fine structure lines, whereas the H₂ S(1) and S(3) transitions were obtained using the SWS (de Graauw et al. 1996) AOT02 grating mode. The [C II] and H₂ observations show unresolved line profiles, while the [O I] spectra only yield upper limits, as summarized in Table 3. The reduction was performed with the LWS version 6.0 pipeline software and the SWS reduction package (Thi 1997, private communication). The detection of the S(1) and S(3) pure rotation H₂ lines indicates warm (T > 200 K) gas. This result will be further explored through the physical models constructed below.

Table 3
ISO Observations of Ced 201

Line	I	$\theta_{ m beam}$
	${ m W~m^{-2}}$	
[C II] (158 μ m)	3.80×10^{-15}	90"
[O I] (63 μ m)	$<8\times10^{-15}$	90"
$H_2 S(1) (17 \mu m)$	1.10×10^{-16}	$14'' \times 27''$
$H_2 S(3) (9 \mu m)$	5.61×10^{-17}	$14'' \times 20''$

2.4. Comparison with Other Lines of Sight

Before discussing the construction of specific models for Ced 201, it is good to compare the observed [C II] 158 μ m line intensity, which accounts for 50% of the total cooling rate in moderate density PDRs ($n_{\rm H} < 10^4~{\rm cm}^{-3}$), with other lines of sight. The above value translates into $2 \times 10^{-5}~{\rm erg~s}^{-1}~{\rm cm}^{-2}~{\rm sr}^{-1}$, which should be compared to 2.2×10^{-3} for W3 (Boreiko, Betz, & Zmuidzinas 1993) and 4.6×10^{-4} for S140 (Minchin et al. 1994). Because the [C II] flux scales roughly linear with the impinging UV flux in this regime, care should be taken in comparing these numbers. It will be shown below that the strength of the

incident radiation in interstellar units is $G_0 = 200$ for Ced 201, roughly equal to the S140 value, whereas W3 is characterized by $G_0 \sim 5 \times 10^3$. With these numbers one finds that the Ced 201 [C II] line is underluminous. The remaining difference between the various lines of sight, and the topic of this work, is the shape of illuminating radiation field.

Since the effective temperature of the illuminating star is 10,000 K, whereas it is $\sim 30,000$ K for S140 and W3, one would expect Ced 201 to be well described by cool PDR models. These exhibit a much smaller [C II]/CO ratio for the higher rotational levels of CO, $J \geq 3$ (Spaans et al. 1994). The reasons are that 1) the soft radiation field causes lower temperatures and hence smaller collisional excitation rates, and 2) the abundance ratio C⁺/CO is much larger in a soft UV field since C ionization and CO dissociation occur in the 912-1110 Å wavelength range. Indeed, the [C II] line flux is not only small in Ced 201, which by itself may be due to abundance, temperature, and (column) density effects, it is also small compared to the observed CO 3-2 line with a ratio of about 100. This is roughly an order of magnitude smaller than the corresponding ratios for the other lines of sight. The fact that the high temperature [O I] 63 μ m line, at an excitation temperature of about 228 K above ground, is not detected at all toward Ced 201, is consistent with these results if the gas temperature is smaller than 150 K throughout most of the cloud (see the PDR models below).

3. A Physical Model for Ced 201

The analysis of the data and construction of a physical model for Ced 201 will proceed in several steps. First, the average density, temperature and abundances of observed species are determined from the observations through a simple excitation model. The chemical abundances are then reproduced through iteration of more elaborate 1D and 3D PDR models, which incorporate the chemical and thermal balance of the medium, and the geometry of the reflection nebula. The motivation for the latter is that the spatial variations in the temperature and chemical abundances strongly influence the observed line intensities.

The intensities of emission lines are determined by the level populations and optical depth along the line of sight. A one-dimensional escape probability radiative transfer code has been applied to determine these quantities for the detected lines. The code includes collisional and radiative (de-)excitation processes, and computes the level populations and line optical depth for a given set of physical parameters: density, temperature, column density, line width, and the temperature of the cosmic microwave background. Comparison with the observed intensities then results in a first guess for the beam-averaged kinetic temperature, density and column density of the observed species. This radiative transfer code and the procedure for analyzing the data has been described in Jansen, van Dishoeck & Black (1994) and Jansen (1995). In Table 4 the derived physical parameters are summarized. The kinetic temperature and the density of the main collision partner, molecular hydrogen, have been determined using the line intensities of the ¹²CO and ¹³CO transitions. The optically thick ¹²CO lines were used to constrain the kinetic temperature, i.e. this is the temperature of the (self-shielding) molecular gas, whereas the ¹³CO 3-2/2-1 line ratio was used as the main density probe (see Figure 8a of Hogerheijde et al. 1995).

 $\label{eq:Table 4}$ Physical Parameters and Column Densities of Ced 201

T	$(40 \pm 10) \text{ K}$
$n(\mathrm{H}_2)$	$(5000 \pm 1000) \text{ cm}^{-3}$
N(CO)	$(2\pm1)\times10^{17}~{\rm cm}^{-2}$
$N(^{13}CO)$	$(3 \pm 1) \times 10^{15} \text{ cm}^{-2}$
N(CI)	$< 2 \times 10^{16} \text{ cm}^{-2}$
$N(\mathrm{CII})$	$(4 \pm 2) \times 10^{17} \text{ cm}^{-2}$
$N(\mathrm{C^{18}O})$	$< 4 \times 10^{13} \text{ cm}^{-2}$
$N(\mathrm{HCO^+})$	$(8 \pm 3) \times 10^{11} \text{ cm}^{-2}$
N(CS)	$< 1 \times 10^{12} \text{ cm}^{-2}$
N(OI)	$< 4 \times 10^{18} \text{ cm}^{-2}$

It is important to realize that the C⁺ column density is quite sensitive to the temperature structure of the cloud due to its excitation temperature of 92 K. For the 1D and 3D models we shall therefore compare to the observed flux directly. Since the more detailed models discussed below provide a good fit to the observed line strengths, and indicate column densities quite similar (within the errors) to the one above, we will use this knowledge and the value of the C⁺ column density to derive now the gas phase carbon abundance.

The gas phase carbon budget is dominated by 12 CO, C and C⁺. The sum of the derived column densities yields for the column density of gas phase carbon $N(^{12}$ C) = $(6 \pm 2) \times 10^{17}$ cm⁻². If it is assumed that the central gas cloud of Ced 201 is spherical, then one can compare the gas phase carbon column density with the column density of hydrogen nuclei $(N_{\rm H})$ along the line of sight. For spherical symmetry, $N_{\rm H} = n_{\rm H} \times diameter = (7.6 \pm 2.3) \times 10^{21}$ cm⁻², where the diameter from the 12 CO 2-1 map is 120" at 420 pc, and the error is

dominated by the non-circularity of the map. Thus, one finds for the gas phase carbon abundance $A(C) = (1.2 \pm 0.4) \times 10^{-4}$. The cosmic abundance of carbon is $\approx 4 \times 10^{-4}$. Note here that the cosmic abundances are thought to be 30% lower than the Solar abundances (c.f. Meyer 1997). One finds for Ced 201 that the fraction of carbon in the gas phase is 35% \pm 10%. For diffuse clouds a gas phase carbon abundance of 1.4×10^{-4} is derived based on GHRS/HST observations (Cardelli et al. 1993), consistent with the result found here.

If one assumes a carbon abundance of 10^{-4} , that C⁺ is the dominant carbon bearing species in the atomic PDR zone, and that the ambient density is above the critical density of $\sim 3 \times 10^3$ cm⁻³ (LTE) as motivated by the detected CO emission, then the size of the emitting region and the energy rate per hydrogen nucleus required to reproduce the observed line flux can be estimated. Clearly, various combinations of size and energy rate per H atom will yield identical line luminosities. Still, in LTE one cannot increase the emitted flux by a large amount unless the ambient temperature is below the excitation temperature, in which case the line would be quite weak. Therefore, taking a size of $\sim 120''$ from the CO and IRAS dust maps, one cannot make the [C II] emitting region much smaller than this without violating the observations, i.e. above 92 K per collision one increases mostly the ambient temperature and not the line luminosity. From these considerations it follows (to first order) that the beam filling factor of the emitting gas is roughly unity and the ambient temperature in the [C II] emitting region is not less than the excitation temperature of 92 K.

3.1. The 1D PDR Model

Previous studies of PDRs illuminated by a (interstellar) radiation field with an effective temperature of about 30,000 K have been performed by Tielens & Hollenbach (1985); van Dishoeck & Black (1988); Burton et al. (1990); Hollenbach et al. (1991); le Bourlot et al.

(1992); Störzer, Stutzki, & Sternberg 1996; at various levels of sophistication. Spaans et al. (1994) extended PDR calculations to softer ($T_{\rm eff}=20,000-6,000~{\rm K}$) radiation fields in order to study the changes in the photo-electric heating efficiency. In this work two different models valid for clouds illuminated by an intense but soft radiation field, the 1D PDR model and the 3D PDR model, will be applied to, and tested for, Ced 201.

The one-dimensional PDR model is an extension of the diffuse cloud model of van Dishoeck & Black (1986) and is thoroughly described in Jansen et al. (1995, also referred to as the Leiden PDR model). In this model, the PDR is described as an infinite plane parallel slab in thermal and chemical equilibrium with a radiation field incident from one side. The calculation of the chemical conditions in the PDR is performed in spatial steps, where the radiation field at a certain point is determined by calculating the attenuation by dust grains, and optical depth effects in the UV absorption lines of H₂ and CO which lead to dissociation. Moreover, shielding of CO by overlapping H₂ absorption lines (mutual shielding) is also taken into account (van Dishoeck & Black 1988). The chemical network includes 215 different species, based on 24 elements and the isotopes of H, C and O (Jansen et al. 1995). The thermal balance is calculated simultaneously with the chemistry. The heating processes include photo-electric heating by dust grains and PAHs (Bakes & Tielens 1994), heating by cosmic rays ($\zeta = 5.0 \times 10^{-17} \text{ s}^{-1}$), H₂ formation heating, carbon photo-ionization heating, and collisional de-excitation of vibrationally excited H₂ (Tielens & Hollenbach 1985; Sternberg & Dalgarno 1989). Cooling is provided by spontaneous decay of collisionally excited fine-structure levels of C⁺, C and O, and rotational levels of CO.

3.2. The 3D PDR Model

In addition to the one-dimensional PDR model, the three-dimensional model developed by Spaans (1996), hereafter referred to as the 3D PDR model, is applied to Ced 201. Analogous to the 1D PDR model, this model calculates the thermal and chemical balance of the cool PDR, using the stellar radiation field, the morphology, the elemental abundances and the (constant) density as input parameters. Nevertheless, differences between the models occur, due to the geometry, radiative transfer and chemical network. The radiative transfer in the 3D PDR model is extended from one to three dimensions, thus enabling the interpretation of line intensities from geometrically more complex clouds and to take into account the position of the illuminating star. Furthermore, the interstellar radiation field (ISRF, Draine 1978) is explicitly taken into account as an isotropic background radiation field illuminating the side of the cloud opposite to the star.

In contrast with the escape probability method of the 1D PDR model, the 3D PDR model uses Monte Carlo radiative transfer (Spaans & van Langevelde 1992; Spaans 1996). According to this method, the PDR is divided in a large number of different cells with a typical size no larger than the mean free path of a photon. The physical conditions differ in each cell, thus influencing the excitation of atomic and molecular lines. Calculation of the radiative transfer proceeds by determining the stimulated emission and absorption (line and continuum) for propagating photon packages in each cell simultaneously. Spontaneous emission of line photon packages occurs in random directions. The chemical network incorporated in the 3D PDR model is more limited, and includes only the \sim 40 most important observable species. Nevertheless, the network is shown to be detailed enough to model the C⁺/C/CO transition accurately (Spaans & van Dishoeck 1997).

4. Results

Since the central gas cloud and the illuminating star are located in the same direction, the abundances as a function of visual extinction, calculated by the models, can be directly converted into column densities by integrating over the total extent along the line of sight. The aim of the constructed models is to reproduce the observed column densities, in particular the gas phase carbon column density $N(^{12}\text{C})$, the [C II] and [O I] line intensities, and to determine the best fit input parameters of the 1D and 3D models.

Table 5 summarizes the input parameters resulting in the best fit 1D PDR model. The illuminating radiation field is determined by considering the central star as a black body with $T_{eff} = 10{,}000$ K, placed at a distance of $R_{nebula} = 0.4$ pc. This corresponds to a value of $G_0 = 200$ in units of the average interstellar radiation between 13.6 and 2 eV (Spaans et al. 1994), which is derived from the spectral type of the star and the infrared observations presented by Casey (1991) in a straightforward manner. The density of hydrogen nuclei in Ced 201 is found to be $n_{\rm H}=2n({\rm H_2})+n({\rm H})=1.2\times10^4~{\rm cm^{-3}}$ and reproduces well the observed chemical abundances. The best fit column density of molecular hydrogen $N({\rm H_2}) = 1.6 \times 10^{21}~{\rm cm^{-2}}$ is a measure of the physical size of the cloud. When compared with the spherically symmetric case, $N({\rm H_2})_{\rm sph.symm.} = 3.8 \times 10^{21}~{\rm cm}^{-2}$, its value indicates that the PDR is flattened along the line of sight. Note that this also implies that the abundance of gas phase carbon must be higher than 35%. In fact, the flattened geometry yields 80% for the abundance of carbon in the gas phase relative to the cosmic abundance. This revised gas phase abundance is thus a factor of two higher than the value of 1.4×10^{-4} found for diffuse clouds. The best fit model also constrains the gas phase abundances δ of several other elements, which are shown in Table 5. The gas phase fraction of nitrogen is rather arbitrarily chosen, since no observations of nitrogen bearing species were obtained.

Table 5
Input Parameters for the Best
Fit of the 1D PDR Model

$R_{ m nebula}$	0.4 pc
$n_{ m H}$	$1.2 \times 10^4 \ {\rm cm}^{-3}$
$N(\mathrm{H}_2)$	$1.6 \times 10^{21} \ \mathrm{cm^{-2}}$
δC	0.80
$\delta { m O}$	0.80
$\delta \mathrm{S}$	0.01
$\delta { m N}$	0.70
δ metals	0.02

The 3D PDR model is applied consistently with the 1D PDR model. That is, the only input parameter of the 3D PDR model which can be modified for a constant density cloud is the three-dimensional geometry of the cool PDR. The best reproductions of the observed column densities are obtained for an oblate ellipsoid with an axis ratio of 2.4. The 1D and 3D models which yield the best fit to the observations are presented in Table 6.

Table 6
Comparison Between the Observed Column Densities,
the 1D PDR Model and the 3D PDR Model

Species	Observed	1D PDR	3D PDR Model
	${\rm cm}^{-2}$	${\rm cm}^{-2}$	${\rm cm}^{-2}$
H_2	-	1.6×10^{21}	1.5×10^{21}
$^{12}\mathrm{CO}$	$(2\pm1)\times10^{17}$	2.3×10^{17}	2.1×10^{17}
$^{13}\mathrm{CO}$	$(3\pm1)\times10^{15}$	4.4×10^{15}	3.1×10^{15}
$\mathrm{C^{18}O}$	$<4\times10^{13}$	7.2×10^{13}	3.1×10^{13}
C	$<2\times10^{16}$	5.2×10^{16}	3.2×10^{16}
C^{+}	$(4\pm2)\times10^{17}$	3.2×10^{17}	3.7×10^{17}
CS	$<1\times10^{12}$	6.3×10^{11}	5.1×10^{11}
HCO ⁺	$(8 \pm 3) \times 10^{11}$	4.1×10^{11}	6.8×10^{11}

4.1. Chemical Structure

The 1D PDR model yields the abundances as functions of depth for approximately 200 species, of which the most important ones are plotted in Figure 2. The assumed isotope ratios are $[^{12}C]/[^{13}C] = 60$ and $[^{16}O]/[^{18}O] = 500$. At the illuminated side of Ced 201, ionized carbon is the dominant carbon bearing species. Due to line shielding and attenuation by intervening dust, the ionized carbon is converted into neutral carbon and carbon monoxide at $A_V \sim 1$ mag (Tielens & Hollenbach, 1985, Black & van Dishoeck, 1987, and references therein). Nowhere in the cloud does neutral carbon become the dominant carbon bearing species.

The abundances of several species determined by the 3D PDR model are shown in Figure 3. Consistent with the 1D PDR model, the $C^+/C/CO$ transition occurs at an

extinction of $A_V \sim 1$ mag. Due to the ISRF which illuminates the cloud from all directions, a second C⁺/C/CO transition zone is present at $A_V \sim 2$ mag on the far side of the PDR. Atomic hydrogen is the dominant form of hydrogen at the illuminated edge, but the shielding of H₂ is very efficient and leads to a sharp transition.

4.2. Thermal Balance and Small Grains

Both the 3D PDR model and the 1D PDR model compute the thermal balance in Ced 201. Figures 4 and 5 show the heating and cooling rates as functions of depth determined by the 1D PDR model. Except for the heating by cosmic rays, all heating mechanisms decrease with depth into the cloud. Photo-electric emissions by PAHs and dust grains are the dominant heating mechanisms in Ced 201. The heating rates of these two processes are equal, although only 10 % of the solid state carbon is incorporated into PAHs in the best fit model. This shows how quantum effects in PAHs can contribute significantly to the heating process in cool radiation fields (Bakes & Tielens, 1994). Cooling is provided by radiative decay of collisionally excited species. The cooling rates due to the main coolants are shown in Figure 5, and depend strongly on the abundances of these species. The observations do not provide good constraints on the column density of atomic oxygen, and a gas phase fraction of 3.2×10^{-4} is therefore assumed (Meyer 1997).

The thermal balance is established at an equilibrium temperature profile determined by the heating and cooling rates. Figures 6 and 7 show these profiles for the 1D PDR model and the 3D PDR model, respectively. The temperature profiles calculated by both models are approximately the same. The temperature at the illuminated edge is 168 K according to the 3D PDR model, and 169 K for the 1D PDR model. The temperature decreases with increasing depth, and is for both models ~ 40 K at $A_V = 1$ mag, where the temperature tracer carbon monoxide becomes abundant. According to the 1D PDR model,

the temperature gradually declines at the dark side of the PDR. Due to the ISRF however, the 3D PDR model predicts that the temperature will increase again, after reaching its minimum of 22 K at $A_V = 1.8$ mag, and becomes 34 K at the dark side of Ced 201.

For the best fit models to the chemical abundances, one can determine the model dependent, i.e. with the distance to the star fixed by the infrared observations, contribution to the heating rate from PAHs and VSGs. The models indicate that 10% of the gas phase carbon is locked up in the form of PAHs, i.e. $D_{\text{PAH}} = 0.1$, where PAHs are defined as any carbonaceous particle of linear size less than 15Å. Additional models were run without any contribution of PAHs and VSGs to check the robustness of this result. The resulting thermal balance in the latter case yields temperatures at the edge of the cloud which are lower by 50%, and strongly underestimates the observed [C II] flux. The fraction $D_{\text{PAH}} = 0.1$ also yields good agreement with the observed CO excitation temperatures. The precise value for D_{PAH} depends on the model. Nevertheless, a firm conclusion is that heating by PAHs and VSGs is required to explain the observed properties of Ced 201, provided no heating sources other than photo-electric heating and cosmic rays are important.

A final crucial comparison comes from the predicted [C II] 158 μ m and [O I] 63 μ m line intensities, because they reflect the thermal balance of the medium most strongly. In the 1D case one finds values of 1.1×10^{-5} for [C II] and 1.9×10^{-5} erg s⁻¹ cm⁻² sr⁻¹ for [O I]. The 3D results are systematically higher and yield 1.8×10^{-5} and 2.7×10^{-5} erg s⁻¹ cm⁻² sr⁻¹, respectively. Comparison with the observed [CII] intensity would thus favor the 3D model, but the difference is small.

4.3. Pure Rotational H₂ Lines

The H₂ J=3 and J=5 levels in the vibrational ground state lie at $\sim 1,000$ K and $\sim 2,500$ K above ground, and therefore trace warm molecular gas. The ISO observations of the H₂ S(1) and S(3) pure rotational transitions are not included in the PDR models, since at kinetic temperatures of T < 100 K, i.e. in a large part of Ced 201, the absolute intensities of these lines are negligible. For higher temperatures these lines are useful temperature tracers because they are optically thin and the level populations are in thermal equilibrium. The ratio between the observed transitions is $I(9\mu\text{m})/I(17\mu\text{m}) = 0.69$, which indicates a kinetic temperature of $T \sim 330$ K (Black & van Dishoeck 1987).

This observational result is clearly at variance with the model predictions. Particularly since the effective temperature of the illuminating is low. It appears that an additional heating source is required in some part of the cloud. If we assume that a thin layer of hot gas is present at the illuminated edge or any where else inside the cool PDR, then it follows from the absolute intensities that this layer is not thicker than $\delta A_{\rm V} \sim 0.05$ mag for a mean H₂ fraction of 0.2. We therefore feel that the value of $D_{\rm PAH}$ remains secure since the chemical constraints which enter into it, derive from regions in the cloud with $A_{\rm V} > 0.3$ mag. The upper limit of 5×10^{-5} erg s⁻¹ cm⁻¹ sr⁻¹ for the [O I] 63 μ m line and its density dependence of $1.0 \times 10^{-8} n_{\rm H_2}$ erg s⁻¹ cm⁻¹ sr⁻¹ for temperatures higher than 228 K and subthermal excitation, indicate that an upper limit for the H₂ gas density of 5×10^3 cm⁻³ when a unity beam filling factor is adopted. ¿From the CO maps we estimate a beam dilution factor of not more than two, so the upper limit is consistent with the CO density estimate and vibrational de-excitation heating by H₂ can be ruled out.

Furthermore, the continuum intensity observed by IRAS is around 2×10^{-3} erg s⁻¹ cm⁻² sr⁻¹, whereas the [C II] intensity is 2×10^{-5} erg s⁻¹ cm⁻² sr⁻¹. This translates into a heating efficiency for the gas of 1%, a generic value for PDRs. The temperature of 300 K

itself requires a G_0 of 5×10^3 for an ambient H_2 density of 5×10^3 cm⁻³, incompatable with the value $G_0 = 200$ from the illuminating star. All in all, the high temperature molecular gas remains to be explained, and does not seem to be accommodated by the process of photo-electric heating. In fact, observations presented by Witt et al. (1987) on the scattering properties of dust in Ced 201 indicate that there is a narrow size distribution of grains skewed toward larger than average particle sizes. This renders a larger contribution to the photo-electric heating by small grains unlikely.

One might argue that the H_2 levels are populated through UV pumping. Even though the reflection nebula is relatively close to the illuminating star, the low effective stellar temperature strongly quenches the 912-1110 Å flux relative for H_2 fluorescence. A straightforward calculation shows that UV irradiation can account for at most 20% of the S(3) line, thereby rendering it a minor contribution.

An additional heating source like turbulent dissipation could be present in the cool PDR (Falgarone & Puget 1995). This requires the input of kinetic energy on the scale of the cloud, possibly through a weak (3-5 km s⁻¹) shock. A C-shock of 7 km s⁻¹ into a gas of pre-shock density 10^4 cm⁻³ would also suffice, but would likely lead to an observable [O I] 63 μ m line. Finally, the case of Ced 201 appears not to be unique. Observations obtained by Timmermann et al. (1996) for S140 indicate similarly warm gas. It would be quite interesting if more of such warm regions show up in H₂ rotational line data.

5. Conclusions

The 1D PDR and the 3D PDR model reproduce the chemical abundances and the thermal balance of the cool PDR Ced 201 as derived from the observations. All observed lines, obtained with the JCMT, ISO and NRAO, are accommodated by these models, except

for the pure rotational transitions of H_2 . The observed H_2 S(1) and S(3) line intensities indicate the presence of hot gas with a kinetic temperature of $T \sim 330$ K, which is probably located in a thin layer of $\delta A_{\rm V} \sim 0.05$ mag at the illuminated edge of the cool PDR. The best fit models indicate that the gas phase carbon abundance is 50% of Solar, and that 10% of the available carbon atoms is in the form of PAHs and VSGs.

Research in astrochemistry in Leiden is supported by the Netherlands Organization for Scientific Research (NWO). MS is supported by NASA through grant HF-01101.01-97A, awarded by the Space Telescope Institute, which is operated by the Association of Universities for Research in Astronomy, Inc., for NASA under contract NAS 5-26555. We are grateful to the assistence of Jante Salverda and Remo Tilanus in obtaining the observations presented in this work. We would like to thank Wing-Fai Thi for the ISO-SWS reduction, Byron Mattingly for obtaining the NRAO 12m observations, and John Black for general discussions and computer codes.

REFERENCES

Bakes, E.L.O., & Tielens, A.G.G.M. 1994, ApJ, 427, 822

Boreiko, R.T., Betz, A.L., & Zmuidzinas, J. 1990, ApJ, 353, 181

Black, J.H. & van Dishoeck, E.F. 1987, ApJ, 322, 412

Burton, M.G., Hollenbach, D.J., & Tielens, A.G.G.M. 1990, ApJ, 365, 620

Cardelli, J.A., Federman, S.R., Lambert, D.L., & Theodosiou, C.E. 1993, ApJ, 416, L41

Casey, S.C. 1991, ApJ, 371, 183

Clegg et al. 1996, A&A, 315,

de Graauw et al. 1996, A&A, 315,

Draine, B.T. 1978, ApJS, 36, 595

Falgarone, E., & Puget, J.-L. 1995, A&A, 293, 840

Hogerheijde, M.R., Jansen, D.J., & van Dishoeck, E.F. 1995, A&A, 294, 792

Hollenbach, D.J., & Tielens, A.G.G.M. 1997, Ann. Rev. Astron. Astrophys., 35, 179

Hollenbach, D.J., Takahashi, T., & Tielens, A.G.G.M. 1991, ApJ, 377, 192

Jansen, D.J. 1995, Ph.D. Thesis, Leiden Observatory

Jansen, D.J., van Dishoeck, E.F., Black, J.H., Spaans, M. & Sosin, C. 1995, A&A, 302, 223

Jansen, D.J., van Dishoeck, E.F., & Black, J.H. 1994, A&A, 282, 605

le Bourlot, J., Pineau de Forêts, G., Roueff, E. & Flower, D.R. 1992, A&A, 267, 233

Meyer, D.M. 1997, in Molecules in Astrophysics: Probes and Processes, IAU 178, (Kluwer:Dordrecht), P. 407

Minchin, N.R., White, G.J., Stutzki, J., Krause, D. 1994, A&A, 291, 250

Spaans, M. 1996, A&A, 307, 271

Spaans, M., Tielens, A.G.G.M., van Dishoeck, E.F. & Bakes, E.L.O. 1994, ApJ, 437, 270

Spaans, M. & van Dishoeck, E.F. 1997, A&A, 323, 953

Spaans, M. & van Langevelde, H.J. 1992, MNRAS, 258, 159

Sternberg, A., & Dalgarno, A. 1989, ApJ, 338, 197

Störzer, H., Stutzki, J., & Sternberg, A. 1996, A&A, 310, 592

Tielens, A.G.G.M., & Hollenbach, D.J. 1985, ApJ, 291, 722

Timmermann, R., Bertoldi, F., Wright, C.M., Drapatz, S., Draine, B.T., Haser, L., & Sternberg, A. 1996, A&A, 315, L281

van Dishoeck, E.F., & Black, J.H. 1986, ApJS, 62, 109

van Dishoeck, E.F., & Black, J.H. 1988, ApJ, 334, 771

Witt, A.V., Graff, S.M., Bohlin, R.C., & Stecher, T.P. 1987, ApJ, 321, 912

This manuscript was prepared with the AAS LATEX macros v4.0.

Fig. 1.— Contourplot of Ced 201. In the left panel the integrated line intensities with spacings of 60" of the $^{12}\text{CO}\ 2 \to 1$ transition are shown. The contours represent values of 0.6, 5, 10, 15, 20 and 25 K km s⁻¹. The right panel presents the integrated line intensities of the $^{13}\text{CO}\ 2 \to 1$ line with spacings of 20". The contour values correspond to 2, 4 and 6 K km s⁻¹. The $^{13}\text{CO}\ 2 \to 1$ emission is also indicated in white in the left panel.

Fig. 2.— Abundances of carbon bearing species in Ced 201 as functions of visual extinction into the cloud, for the 1D PDR model.

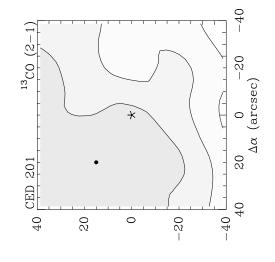
Fig. 3.— Abundances of several species as functions of visual extinction, for the 3D model.

Fig. 4.— The most important heating rates as functions of visual extinction (1D PDR model).

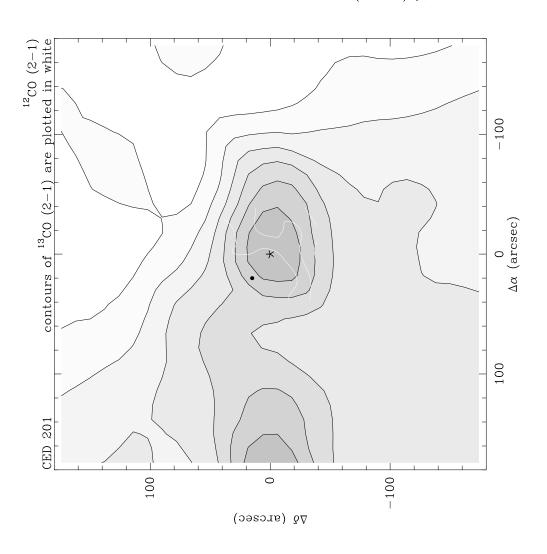
Fig. 5.— Cooling rates originating from the main coolants as functions of visual extinction (1D PDR model).

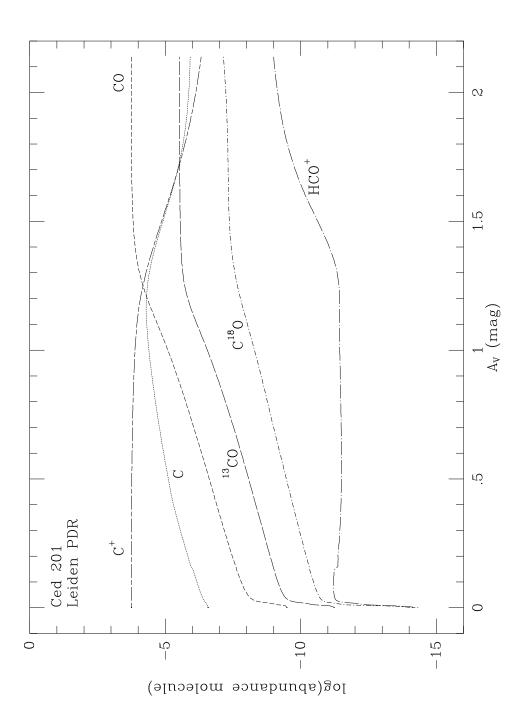
Fig. 6.— Temperature distribution throughout the cloud, according to the 1D PDR model.

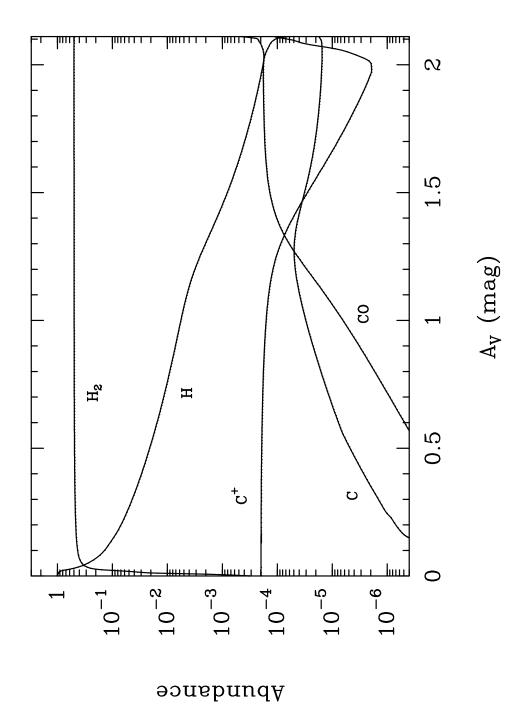
Fig. 7.— The kinetic gas temperature as a function of extinction, according to the 3D PDR model.

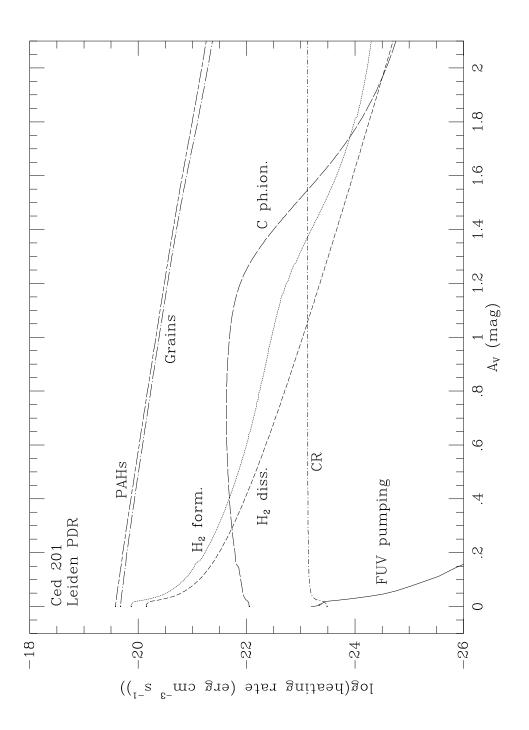


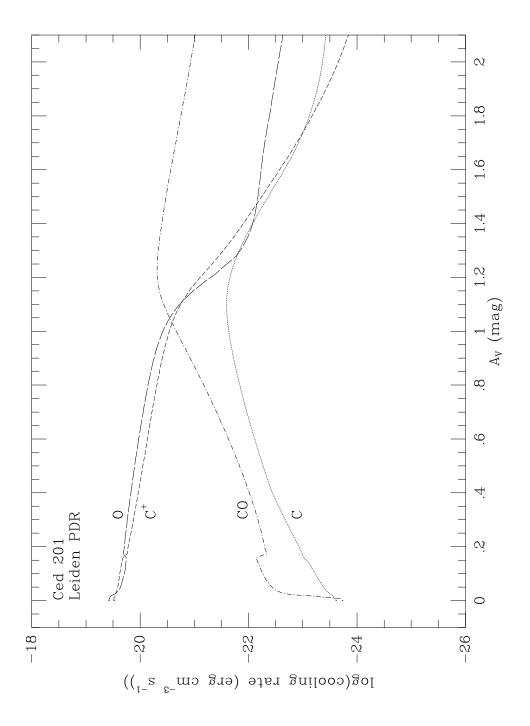
∆δ (arcsec)

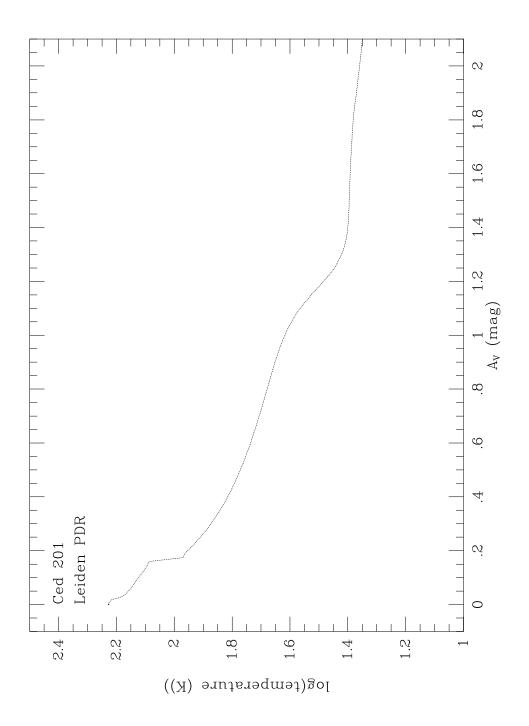


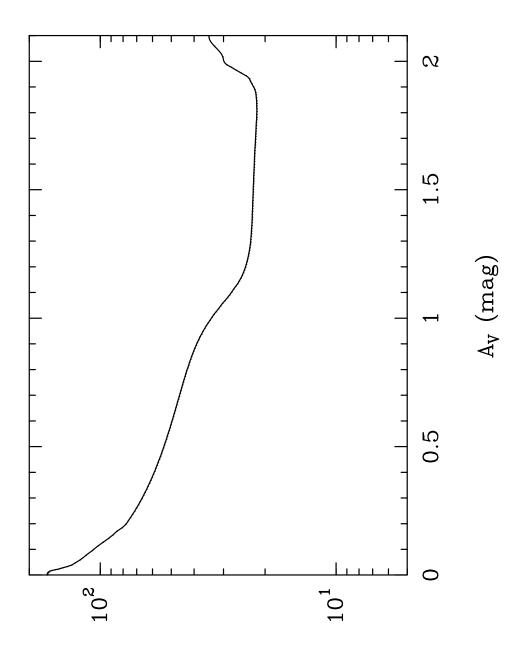












Temperature (K)